Journal Pre-proof

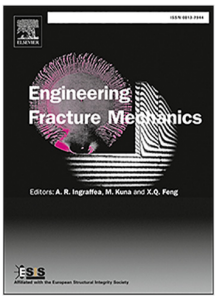

Analysis of prospective SIF and shielding effect for cylindrical rough surfaces obtained by L-PBF

L. Barricelli, S. Beretta

PII: S0013-7944(21)00408-2
DOI: https://doi.org/10.1016/j.engfracmech.2021.107983
Reference: EFM 107983

To appear in: *Engineering Fracture Mechanics*

Received date : 21 May 2021
Revised date : 26 August 2021
Accepted date : 30 August 2021

Please cite this article as: L. Barricelli and S. Beretta, Analysis of prospective SIF and shielding effect for cylindrical rough surfaces obtained by L-PBF. *Engineering Fracture Mechanics* (2021), doi: https://doi.org/10.1016/j.engfracmech.2021.107983.

Analysis of prospective SIF and shielding effect for cylindrical rough surfaces obtained by L-PBF

L. Barricelli[a], S. Beretta[a,*]

[a] *Politecnico di Milano, Department of Mechanical Engineering, Via La Masa 1, I-20156 Milan, Italy*

Abstract

Fatigue properties of parts built by Additive Manufacturing (AM) are strictly related to process-induced defects and complex surface morphology. Several studies have proved that surface valleys act as crack initiation sites, similarly to surface micro-notches. However, different roughness parameters have been considered in literature for the depth of the surface notches, together with the adoption of a shielding factor. The aim of this study is to understand how the surface complexity of L-PBF (Laser-Powder Bed Fusion) AlSi10Mg cylindrical specimens in as-built condition can affect the fatigue behaviour. In detail, CT (Computer Tomography) scans were adopted to characterize the surface quality and 2D FE (Finite Element) analyses were used to calculate the local stress intensity factor at the most critical valleys in the surface. The results of the FE analyses were compared with a shielding factor determined for regularly spaced notches. In spite of the significant scatter, the average geometric factor value for surface notches in L-PBF surfaces is correctly predicted by the traditional shielding factor.

Keywords: AlSi10Mg, computed tomography, additive manufacturing, surface roughness, shielding, FEA

*Corresponding author
Email address: stefano.beretta@polimi.it (S. Beretta)

NOMENCLATURE

a - crack depth

$\overline{a}$ - mean(d_v), average valley depth

a_p - prospective crack depth

AR - average aspect ratio

b - surface pitch

$\overline{b}$ - mean(R_{Sm}), average spacing

d_{gauge} - specimen's nominal gauge diameter

d_v - valley depth

$d_{v,p}$ - prospective valley depth

$d_{vmax,avg}$ - mean value of max valley depth distribution from Block Maxima sampling

F - geometric factor

F_θ - multi-mode geometric factor

$F_{\theta,FEA}$ - geometric factor calculated from multiaxial SIF range results of FE analyses

$\overline{F}_{\theta,FEA}$ - mean geometric factor from FE analysis data

F_{theor} - theoretical geometric factor from Murakami's shielding model

$\overline{F}_{theor}$ - mean value of theoretical geometric factor

i - profile section index

j - crack index

K_I - SIF mode I of a multi-mode crack

K_{II} - SIF mode II of a multi-mode crack

$K_{I,FEA}$ - FE analysis results for mode I SIF

$K_{II,FEA}$ - FE analysis results for mode II SIF

k_I - SIF mode I of a branch crack

k_{II} - SIF mode II of a branch crack

K_f - fatigue notch factor

K_t - elastic stress concentration factor

l_{gauge} - specimen's nominal gauge length

l_e - profile evaluation length

l_s - profile sampling length (length of a section i)

N - number of cycles to failure

R_{eff} - effective stress ratio

R_v - maximum profile valley depth

R_t - maximum profile height

R_c - mean height of profile elements

R_p - maximum profile peak height

R_{sm} - mean width of profile elements

$R_{z,10}$ or $R_{z,ISO}$ - ten point height of irregularities, average maximum profile height

S_v - areal maximum valley depth

S_v - areal maximum surface deviation

$\sqrt{area}$ - crack size equivalent to a defect

$\sqrt{area_R}$ - crack size equivalent to roughness

δ_a - branch crack length

$\Delta\sigma$ - applied stress range

λ_c - cut-off wavelength of profile filter to separate waviness and roughness profile components

λ_s - cut-off wavelength of profile filter for denoising

ρ - linear correlation coefficient

$\overline{\rho}$ - average notch radius

$\sigma_{11,res}$ - longitudinal residual stress

σ_ϵ - standard deviation of the error between FE analysis results and theoretical F data

θ - branch crack inclination angle

Acronyms

μCT - X-Ray micro-computed Tomography

AM - Additive Manufacturing

CT - Computer Tomography

EBM - Electron-beam melting

ESA/ESTEC - European Space Agency / European Space Research and Technology Centre

FE - Finite Element

HCF - High Cycle Fatigue

LEFM - Linear Elastic Fracture Mechanics

L-PBF - Laser-Powder Bed Fusion

SIF - Stress Intensity Factor

1. Introduction

The huge potentiality of L-PBF technologies is now widely recognised by academics and by several industrial fields, such as aerospace, biomedical, automotive, because the additive nature of these technologies makes it possible to produce lightweight parts with a great degree of complexity without tooling and with minimal cost impact. However, there are still some challenges that prevent L-PBF parts from being used for critical applications and surely the *fatigue debit* and the scatter of AM fatigue properties are the most important factors [1], especially considering the implications for qualifying the components [2]. The fatigue debit is the main issue in building functional, load-bearing parts using AM, as most AM components are intended for applications with cyclic loading conditions [3–5].

The complexity of AM parts and the possibility of acting on the process parameters to have a trade-off of material properties (for example, between material densification and surface quality [6]) are sources of a variety of process-related internal and surface flaws, that must be accounted

for when estimating the fatigue properties, especially in terms of size and location distribution, through probabilistic models [7]. As a matter of fact, a huge scatter appears in the fatigue properties of AM parts if the dependence of the fatigue properties on the type, size and location of process defects inside the specimen is neglected [8].

The scatter is actually reduced if a proper model of the fatigue limit as a function of the defect size is considered [9] and a suitable lower-bound of fatigue strength can be estimated considering the size of the largest occuring defects [10] together with their orientation [11].

A damage tolerance approach, within a Fracture Mechanics framework, is often the best engineering choice [1] to correlate part-level fatigue properties to the material's process-induced defects. Flaws are treated as sharp cracks from the very first cycle, because short cracks are very likely to be found at the roots of small defects at the fatigue limit [12], and the fatigue stength estimation is based on the evaluation of the SIF (Stress Intensity Factor) at the crack tips [9, 13].

In the absence of large-enough internal defects that threaten the HCF (High Cycle Fatigue) life, multiple cracks may initiate from the valleys in rough surfaces due to a high crack driving force in these sites [14, 15]. In particular, the fatigue life of as-built AM parts is greatly limited by the surface roughness [16, 17], because the surface is inherently rough due to the additive nature of the process [18] and presents an irregular morphology [19–21].

An as-built L-PBF surface can be seen as a random distribution of micro-notches [22] introducing large stress concentrations and interacting with each other in order to accommodate the local stress field around them. Several methods are proposed in literature to model the effect of the surface quality based on the fatigue behaviour of as-built AM parts, mainly in relation to: stress concentration analysis [23–25], equivalent crack model [5, 26–29], FE analyses [30–33].

Stress concentration analyses are based on the calculation of an "effective" local stress concentration factor for the surface "notches". Schneller et al. [24, 25] adopted a classical definition of the stress concentration factor [34] with the concept of notch sensitivity to estimate K_f, considering the maximum surface deviation S_t and average notch radius $\overline{\rho}$ (calculated considering primary profile [24] or roughness profile [25]) to estimate the fatigue life of as-built L-PBF specimens. Pegues [23] adopted Arola and Ramulu's multi-parameter equations [35] for determining an "effective" elastic stress concentration factor K_t and an "effective" fatigue notch factor K_f for as-built L-PBF Ti6Al4V specimens. However, the equations [35] were derived from a combination of parameters evaluated on an ideal sinusoidal, hence regular, surface profile: for instance, an average curvature radius $\overline{\rho}$ of the valleys is taken to be representative of the period.

Another approach for the surface refers to Fracture Mechanics concepts, similar to those

adopted for fatigue limit estimation in the presence of defects (rough surfaces are treated as "defects"). A short crack approach can be implemented in the fatigue limit estimation [27] together with a model for the shielding of the SIF, like Murakami's model [36] that referred to an "artificial" regular roughness as a periodic series of equivalent 2D cracks Fig. 1.

Beretta et al. [27] proved that the surface effect on the fatigue debit can be well described by a fatigue limit model on the Kitagawa-Takahashi diagram in terms of the size of surface defects observed at the fracture origin and of the effective stress ratio controlled by residual stresses. This approach is able to differentiate between different surface orientations.

Many authors take the "equivalent depth size" to be one of the standard roughness parameters, such as the maximum profile height R_t or R_z [5, 26] or the maximum valley depth R_v [28, 29], for the sake of fatigue strength prediction. Gockel et al. [37] studied properties and performance of L-PBF Inconel718 specimens, focusing on the relationship between the surface roughness parameters and the fatigue life of the as-built specimens printed using different contour parameters. They found a decreasing trend of the fatigue life for increasing values of the max depth of the surface valleys over the evaluation area, i.e. of the areal roughness parameter S_v.

Many authors applied the concept of shielding developed by Murakami for machining grooves idealized with periodical coplanar cracks with a depth a and pitch b, whose geometrical factor F depends on the ratio a/b (see Fig. 1). In any case, both the stress concentration and the Fracture Mechanics approaches lack precision as far as the local behaviour of surface micro-notches is concerned, due to the fact that the periodicity of a machined surface is very different from the random surface of AM processes. In details, oneorus FE-based studies of as-built AM surfaces proved that modelling a regular geometry (assumption at the basis of most Fracture Mechanics studies on roughness) is far from a proper model of the real surface, because the randomness of a real surface requires analyses of local stress concentrations [30–33] .

Few studies tried to adopt more locally-oriented analyses of AM as-built surfaces at the expense of added computational complexity, for example with the help of expensive technology like CT. Du Plessis et al. [38] highlighted the possibility of adopting high-resolution X-Ray CT both for roughness measurements for complex parts, like lattice struts and internal surfaces, and as a basis for simulations to spot highly stressed regions of AM parts.

Buffiere [39] suggested the use of synchrotron tomography with phase contrast in order to detect significative features at sub-pixel resolution and to predict crack initiation through a

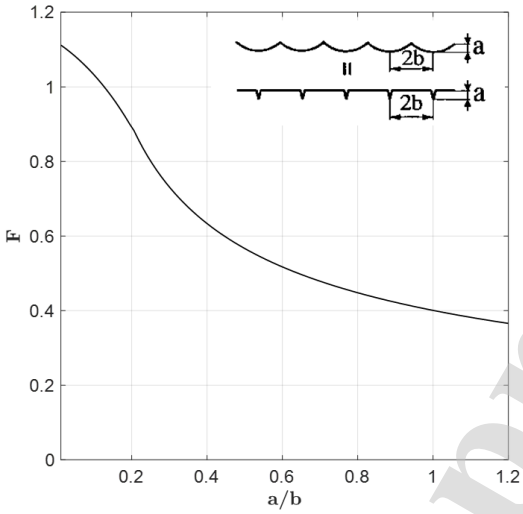

Figure 1: Murakami's expression for the geometric factor in function of the ratio a/b related to a periodic surface profile [36]

mesoscopic approach based on a local stress concentration factor. Persenot et al. [40] used image processing on a flat 3D surface, obtained by "unfolding" radial slices (at a small angular step $d\theta$) from the CT reconstruction of thin EBM (Electron Beam Melting) Ti6Al4V struts. They found that the killer notches were not always the ones with the largest $\sqrt{area}$, but the ones with the smallest curvature radius. Hence, they proposed using a Kitagawa-Takahashi diagram together with a better description of notch-like defects in terms of a stress concentration factor.

Beretta-du Plessis [29] made a direct comparison between the CT-reconstructed 3D specimen's real surface and the best-fit nominal cylinder, to evaluate the most critical surface features. Differently from Persenot, here defect criticality was ranked by means of the SIF at the tip of the deepest valleys, thus supporting the choice of R_v or S_v as relevant roughness parameter.

From this wide literature overview, it is not clear if the shielding model formulation based on periodicity assumptions (see for instance, the regular scheme of 2D cracks in Fig. 1) can really be applied to the surface patterns of as-built AM parts.

1.1. Aims of this paper

A deeper understanding of the AM as-built material's behaviour is necessary for dealing with the AM's surface quality. This study has two main objectives:

- To understand how to model the shielding effect for an irregular surface with a complex morphology and to verify that the roughness parameter R_v is well suited for this purpose.
- To understand how the complexity of the surface morphology affects the presence of multiaxiality in case of a uniaxial loading condition and how these effects can be taken into account for estimating the fatigue properties.

In this work, μCT (micro-computed tomography) was used to analyse a complex L-PBF as-built surface thoroughly. These two main capabilities of μCT were exploited: it captures the surface features well (with an accuracy depending on the resolution, i.e. on the μCT voxel size) [38, 41] and it makes it possible to generate FE models directly from a reconstruction of the real part's geometry [42].

The basic idea was to build 2D FE models from sections of μCT-scanned fatigue specimens in order to investigate the shielding effect on the SIF of small cracks that could be present close to the surface micro-notches of as-built AM specimens. The same μCT scans were used to retrieve surface roughness measurements in order to understand the effect of roughness parameters on the shielding effect and on local multiaxiality near the surface valleys.

2. Materials and methods

2.1. L-PBF AlSi10Mg as-built specimens

A batch of net-shaped L-PBF AlSi10Mg fatigue specimens was provided by ESA/ESTEC to Politecnico di Milano. These specimens are part of a test campaign, whose results were already discussed in [43, 44].

Samples have a gauge section with a length of 11 mm and a diameter of 5.5 mm. The test pieces were built vertically using an EOS M400 machine in vertical orientation, with a layer thickness of 30 μm and a scan strategy (energy input (E) of approximately 50 J/mm^3) that combines an inner hatch pattern with contouring. The build plate was preheated to 165°C during printing. The specimens have an as-built surface condition, as no post-processing surface treatment was applied.

2.2. Residual stresses

Residual stresses were measured at ESA/ESTEC by XRD with a Bruker D8 Dis- cover, a copper (Cu) source at a voltage of 40 kV and a current of 50 lA, a 0.3 mm-collimator, and a 2D detector. The strains were measured at seven points evenly spread out on one line, centred at the gauge and oriented along the longitudinal direction of the specimen (other details in [43, 44]).

The measurements showed a longitudinal surface residual stress $\Delta\sigma_{11,res}$=81 MPa.

2.3. Fatigue properties

As-built specimens were subjected to fatigue tests at $R = -1$ under a 15 kN servohydraulic machine, operating at a frequency of 30 Hz. An S-N curve was obtained by interpolating experimental data from uniaxial fatigue tests at different stress amplitudes with a curve of the type $N = A\Delta\sigma^B$ (standard ASTM E739 [45]). The experimental fatigue limit is $\Delta\sigma_f$=57 MPa. Such a low fatigue strength is due to the presence of the tensile residual stresses, that lead to an effective stress ratio (at the fatigue limit) $R_{eff} = 0.52$, and the surface features of the as built surface.

In most cases, the fracture surfaces revealed the presence of multiple crack initiation from surface defects, similar to those in Fig. 2. The average aspect ratio $AR = a/c$ of the defects was 0.25.

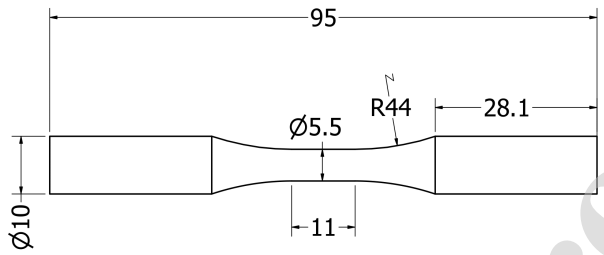

(a)

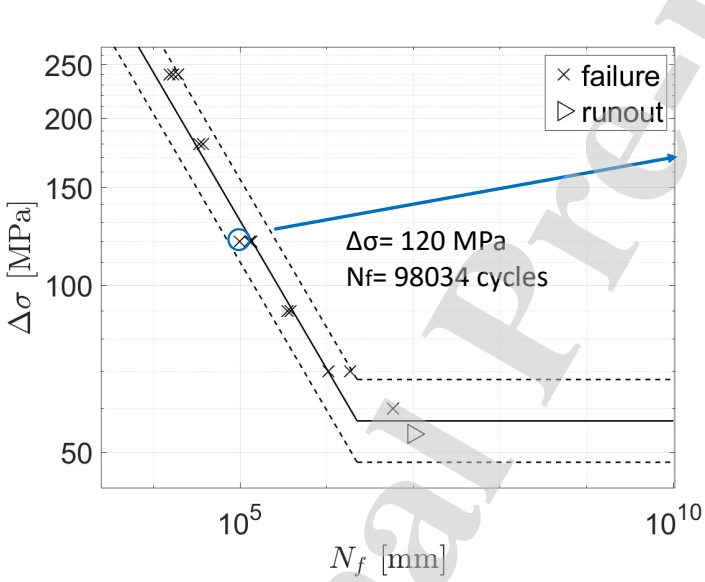

(b)

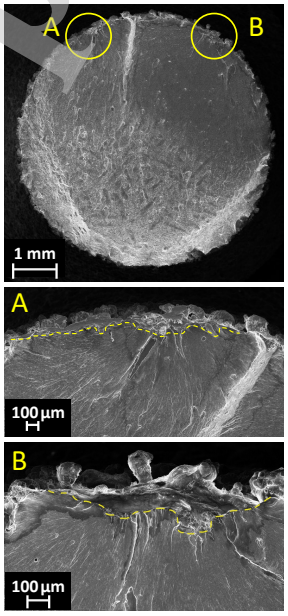

(c)

Figure 2: Fatigue test results: a) geometry of fatigue test specimens according to standard ASTM E466 [43, 46], b) S-N curve of the as-built SLM AlSi10Mg fatigue specimens tested at R=-1, c) details of defects at the fracture origin (multiple loci of fatigue crack initiation).

2.4. CT scans

The μCT scans of two specimens of the as-built AlSi10Mg batch were provided by ESTEC/ESA for this study Fig.3. The CT scans were performed in ESTEC/ESA by a GE Phoenix V|Tome|X. The parameters of the μCT machine included a gun voltage of 230 kV, a current of 100 μA, a Cu filter with a thickness of 0.5 mm, and a timing per frame of 1,000 ms. The voxel size was 8 μm and 1,000 images were acquired over the complete rotation. Data was reconstructed by the Phoenix datos-x (GE) software with optimization to correct artifacts and post-alignment.

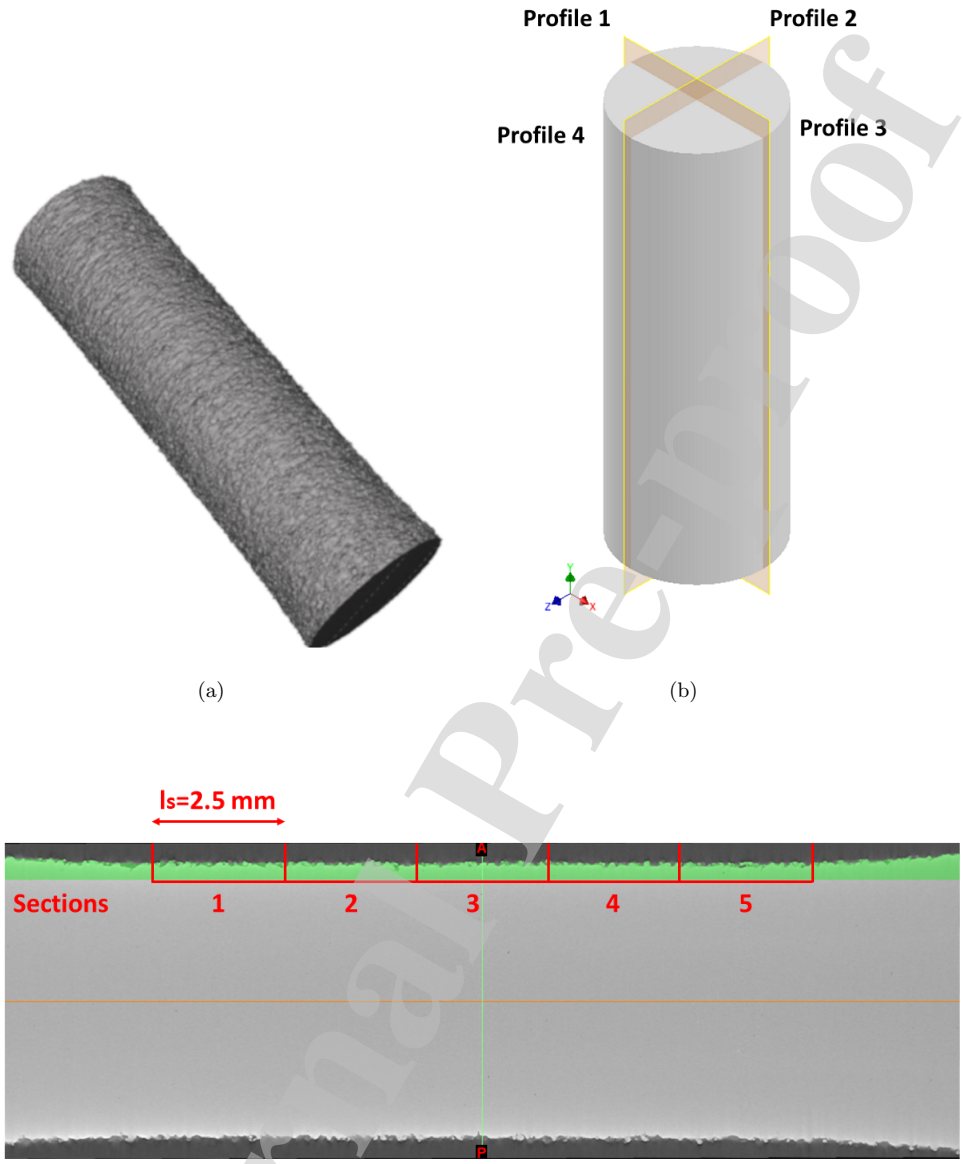

Figure 3: Analysis of as-built specimens: a) μCT 3D reconstruction; b) radial locations of the extracted profiles on the specimen's cylindrical surface; c) cropped and segmented surface profile divided into 5 sections

3. Profile measurements from μCT scan data

3.1. μCT scans post-processing

The post-processing of μCT scans was performed by means of ImageJ (Fiji) and Materialise (Mimics and 3-matic) software packages. After some geometrical transformations to reorient the specimen's reconstructed geometry, two diametral sections (2D slices) were extracted on two planes orthogonal to each other, for each of the two specimens (see Fig. 3).

An image segmentation was performed on Mimics to distinguish the sample's material from the air noise. A ISO50 threshold was applied on the grayscale intensity histogram, with a small manual adjustment to catch the best binary mask of the sample's section. The segmented image was cropped to obtain two profiles per diametral section.

3.2. Measurements from μCT scans

The roughness parameters were evaluated following the profile method included in the ISO 4287 [47] and ISO 4288 [48] standards.

The form is obtained by interpolation of the "ideal" geometrical element, i.e. the reference geometry for the measurement of the profile height deviations, and it has to be removed from the measured profile. For our profiles, the form is the straight line corresponding to the generatrix of the cylindrical specimen's gauge section. The combination of roughness and waviness profiles gives the so-called "primary profile": the two components of the primary profile can be separated by means of a filter [49].

The ISO 3274 standard refers to profile measurements with a contact stylus and prescribes the denoising cut-off wavelength in relation to the stylus tip's radius. In a similar fashion, we chose the denoising wavelength λ_s to be equal to the voxel size of the μCT scans, 8 μm.

A Robust Gauss filter was applied to the measured profile to separate waviness and roughness in order to measure the roughness parameters. The filter was developed in MATLAB using a max allowable error (Euclidean norm of the difference of the profile heights between each iteration and the previous one) as termination criterion and defining a max number of 50 iterations [50].

First, preliminary roughness measurements were taken on a sample profile (one of the 2D profiles extracted from the μCT scan diametral slices) without filtering. The average roughness $R_a = 10 \div 20\,[\mu m]$ led to a choice of a sampling length l_s=2.5 mm and an evaluation length l_e=12.5 mm [48].

Profiles with a total length of 15 mm were then retrieved from the μCT slices, so that the measured profile could be reduced to an evaluation length of l_e=12.5 [mm] after the removal of two half sections at the extremities to avoid end-effects after the filtering step. The evaluation length was then divided in 5 sections with length 2.5 mm, that is the minimum number of sections in terms of the ISO 4287). The fact that that the gauge length $l_g = 11\,[mm]$ is lower than l_e was not a problem, because the Robust Gauss filter does not require removal of the form before its application [51].

After denoising, the surface components were separated by filter iterations with a cut-off wavelength λ_c=2.5 mm. For a first analysis of the results, we calculated the average roughness R_a and the mean spacing parameter R_{Sm} for the roughness profiles obtained after filtering with a cut-off wavelength λ_c=2.5 mm. R_a values fell in the same range $10 \div 20\mu m$, confirming our choice for the filter cut-off wavelength. R_{Sm} was calculated by means of Scott's algorithm [52] (See Appendix 7) and it was found to be in the range $R_{Sm} = 0.2 - 0.3\,[mm]$.

According to ISO4288 [48], this value of R_{Sm} would require a cut-off wavelength of λ_c=0.8 mm. Therefore, we decided to also implement another Robust Gauss filter with λ_c=0.8 mm for analysing the effect of filtering on SIF along the rough profiles.

Table 1 shows some standard roughness parameters calculated over the whole evaluation length (l_e=12.5 mm):

- R_a, arithmetic mean of the deviation of the profile over the evaluation length.
- R_v, maximum profile valley depth over the evaluation length, equal to the maximum value of $R_{v,i}$ (maximum valley depth over a sampling length, i.e. over a section i).
- R_t, total height of the profile (sum of R_v and R_p, where R_p is the maximum profile peak height over the evaluation length).
- R_{sm}, mean width of the profile elements over an evaluation length (mean of the mean widths over each sampling length, $R_{sm,i}$, calculated using the algorithm

proposed by [52], See Appendix A).

- R_{z10} (also R_{zISO}), ten point height of irregularities, difference in height between the average of the five highest peaks and the average of the five lowest valleys of the profile.

The histograms of all the roughness parameters listed above, except R_{z10}, were evaluated also for all the sampling lengths as well (5 sections with a length of 2.5 mm for the filtering with λ_c=2.5 mm, 5 sections with a length of 0.8 mm for the filtering with λ_c=0.8 mm). They are shown in Fig. 4.

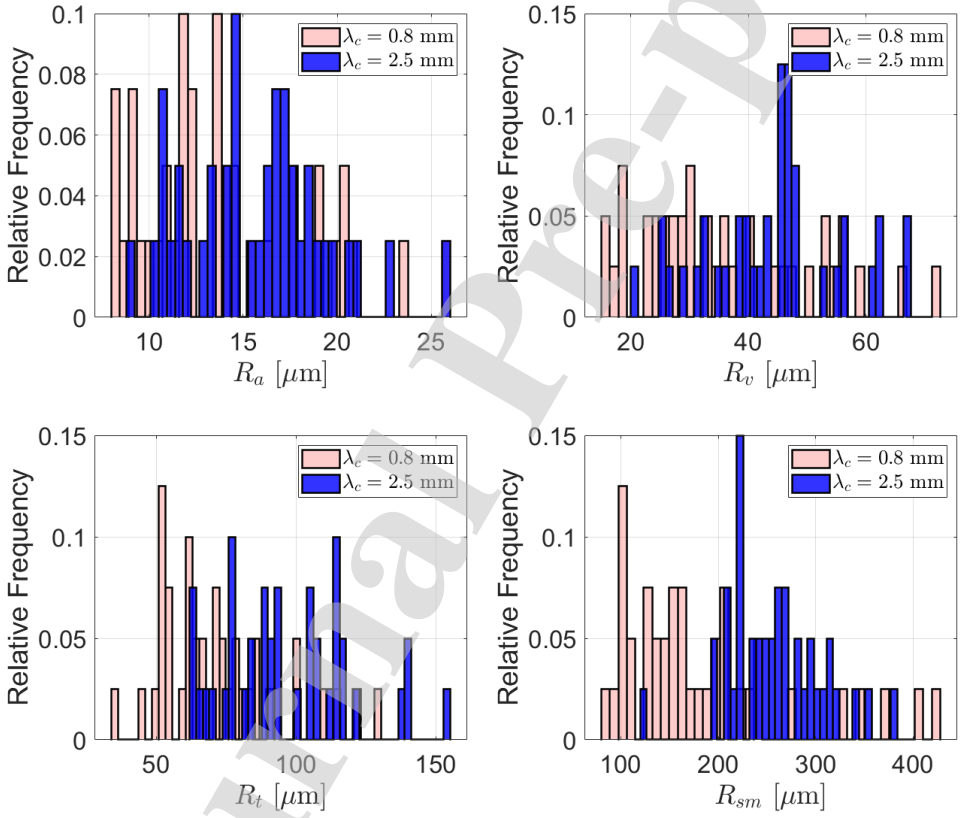

Figure 4: Main standard roughness parameters evaluated for all the sampling lengths.

Table 1: Standard roughness parameters evaluated on the evaluation length of the Gauss-filtered roughness profiles ($l_e = 4mm$ for λ_c=0.8 mm, $l_e = 12.5mm$ for λ_c=2.5 mm)

		$R_a[\mu m]$	$R_v[\mu m]$	$R_t[\mu m]$	$R_{sm}[\mu m]$	$R_{z10}[\mu m]$
Specimen 1 - profile 1	λ_c=**0.8 mm**	14.7	84.4	157	137	106.5
	λ_c=**2.5 mm**	16.3	78.7	152.5	158	107.7
Specimen 1 - profile 2	λ_c=**0.8 mm**	17.9	80	170	141	133.3
	λ_c=**2.5 mm**	19.5	75.9	172.2	148	129.3
Specimen 1 - profile 3	λ_c=**0.8 mm**	16.3	66.7	148.9	211	115.1
	λ_c=**2.5 mm**	18.6	63.2	161.7	176	119.6
Specimen 1 - profile 4	λ_c=**0.8 mm**	16.1	85.5	164.7	169	110
	λ_c=**2.5 mm**	17.9	78.8	151.4	108	105
Specimen 2 - profile 1	λ_c=**0.8 mm**	13.5	58.4	119.3	218	89.9
	λ_c=**2.5 mm**	15.6	45.4	106.7	124	87.5
Specimen 2 - profile 2	λ_c=**0.8 mm**	10.5	53.3	99	183	80.4
	λ_c=**2.5 mm**	11.8	54.3	99.5	114	79.2
Specimen 2 - profile 3	λ_c=**0.8 mm**	9.4	33.2	81.1	185	62.6
	λ_c=**2.5 mm**	10.7	34.2	87.9	130	68.1
Specimen 2 - profile 4	λ_c=**0.8 mm**	13.5	67.7	160.3	244	106.4
	λ_c=**2.5 mm**	15.3	64.4	155.6	128	106.7

4. Finite element analyses

4.1. Extraction of significant profile features for FE analyses

The SIF of the most significant surface features were obtained from FE models of the 2.5 mm-sections extracted from CT scans.

The criterion used for spotting the most critical valleys of the specimen's surface (where short cracks are likely to be present) was to look at deepest valleys. In detail, along each profile, the valleys with depth equal to $R_{v,i}$ were chosen together with a number of other valleys with a depth $d_v = 0.9 - 1.0\, R_v$.

4.2. 2D FE analyses of rough profiles

The 2.5 mm-long sections of the eight surface profiles extracted from CT scans were also imported into the Sketch tool of the ABAQUS CAE package to build 2D parts to be analysed by FE analysis (see Fig. 5).

The loading condition is a uniform unitary traction (σ=1 MPa) to the left edge of the section. The imposed boundary conditions are simple supports on the bottom edge and on the right-side edge of the 2D part.

Each crack, in the significant valleys, was modelled as a 2D crack with a fixed small depth of 5 μm ahead of the real profile depressions. The choice of crack size was driven by the need to consider cracks lower than the surface depressions, in order to catch the effect of local stress concentrations. Considering that size measurements of the order of sub-voxel resolution can be obtained from μCT-scans with good quality and high contrast [53], a crack size close to half the voxel size seemed to be a good compromise (also for a repeatable mesh construction).

The FE model's mesh (quad plane strain quadratic elements, CPE8) was refined close to the surface, with further refinement close to the crack's tip (600 elements within a circular partition with diameter 2.5 μm) in order to have stability of the results (see Fig. 5.c).

A static general step was set up and a history output was requested at each crack, to calculate SIF using the J-integral method [54] on a number of 30 contours.

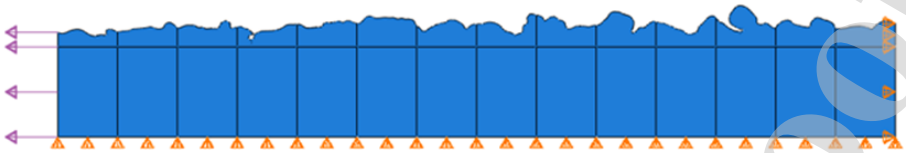

(a)

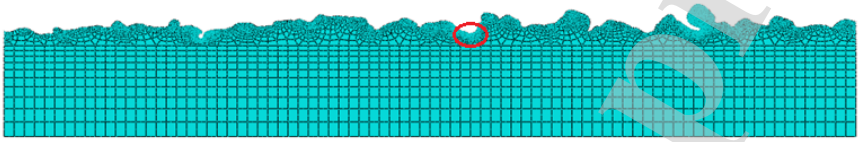

(b)

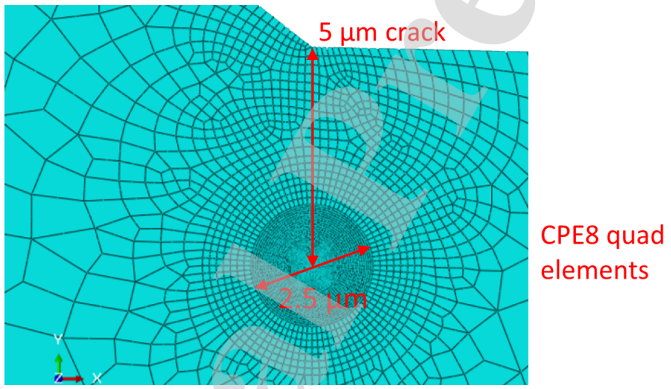

(c)

Figure 5: a) FE analysis - Loading and boundary conditions; b) 2D mesh (refinement near the surface valleys and cracks placed at the deepest valleys); c) Detail of 2D crack modelled at the root of a deep valley

4.3. Simplified approach for multiaxiality effect

The complex morphology of as-built AM surfaces influences the presence of short cracks at the surface valley roots that are subjected to local multiaxial effects, even when the remote applied stress is uniaxial and in presence of multiple cracks.

Crack branching may occur from a mixed-mode initial crack and, if LEFM (Linear Elastic Fracture Mechanics) is applied, the branching direction (inclination angle θ) is completely defined by the equation:

$$\tan\left(\frac{\theta}{2}\right) = \frac{1}{4}\left[\frac{K_I}{K_{II}} \pm \sqrt{\left(\frac{K_I}{K_{II}}\right)^2 + 8}\right] \tag{1}$$

where K_I and K_{II} are the SIF in mode I and mode II of the initial crack. This equation derives from the MTS criterion, according to which the crack branch direction is the one that maximizes the Mode I SIF ahead of the initial crack [55].

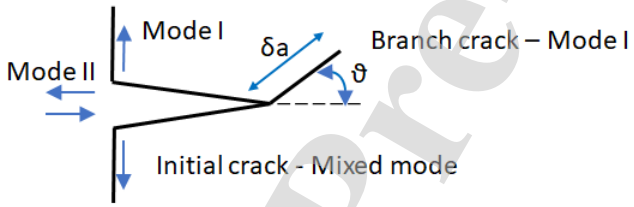

Figure 6: Crack branching from an initial crack in mixed mode (Mode I + Mode II)

Eq. (1) was applied to the values of $K_{I,FEA}$ and $K_{II,FEA}$ (SIF of the crack in mode I and mode II) that were calculated by FE on the last contour around the crack tip, the most stable one. Once θ had been maximized, then the maximum Mode-I SIF along that direction can be calculated as:

$$K_{\theta,FEA} = \frac{0.83K_{I,FEA} + \sqrt{0.4489K_{I,FEA}^2 + 3K_{II,FEA}^2}}{1.5} \tag{2}$$

that represents the maximum prospective SIF ahead of the modelled cracks.

4.3.1. Verification of the $K_{\theta,FEA}$ approach

The approach for determining $K_{\theta,FEA}$ described in the previous section is a simplified way for estimating the prospective SIF ahead of the surface depression, because natural

cracks emanating from the surface notches would not propagate for 5 μm in a vertical direction and then abruptly branch along the direction of maximum tangential stress.

The approximation of the simplified modelling was verified by means of a two-stage FE analysis for some cracks that showed a relevant effect of multiaxiality, as follows:

1. In the first stage of the verification, a new FE model of the section was built by modelling a 3 μm-crack at the critical valleys' root, with an inclination that follows the slope of the valley's edge. The 3 μm-crack was assumed to be the main crack in a multiaxial condition: the SIF ranges in mode I and mode II were extracted from the FE analysis results and introduced in Eq. 1 (Sect. 4.3) to evaluate the crack branch inclination angle θ.
2. In the second stage, another FE analysis was performed to model crack advance. A branch with inclination angle θ was added at the tip of the main 3 μm-crack to reach a total crack depth of 5 μm. The maximum Mode I SIF for the brach crack $k^*_{I,FEA}$ was calculated from the FE analysis results again using Eq. (1) and (2).

A comparison could be performed for four cracks between the values of $k^*_{I,FEA}$ (from the accurate double-stage FE analysis) and the values of $K_{\theta,FEA}$ (calculated with the simplified approach, using SIF ranges at the 5 μm-cracks of the original FE model).

A percentage error was evaluated as $e_1 = \frac{|K_{\theta,FEA} - k^*_{I,FEA}|}{k^*_{I,FEA}}\%$. The results of the verification of the multiaxiality approach for the significant cases examined are listed in Table 2. The calculated error for the cases examined is smaller than 3.5 %, so we can assume that our simplified approach (i.e. the 5 μm straight crack) is sufficiently accurate for determining the prospective maximum SIF ahead of the most severe surface valleys.

Table 2: Cases with significant effect of multiaxiality.

Specimen	**Profile**	**Section**	**Crack**	θ [°]	$k^*_{I,FEA}[MPa\sqrt{m}]$	$K_{I,FEA}[MPa\sqrt{m}]$	$K_{II,FEA}[MPa\sqrt{m}]$	$K_\theta[MPa\sqrt{m}]$	$e_1 = \frac{\lvert K_\theta - k^*_{I,FEA}\rvert}{k^*_{I,FEA}}\%$
1	**4**	**i=1**	**1**	17.5	0.010	0.010	-0.002	0.010	3.4
			2	38.3	0.006	0.006	0.001	0.006	0.8
2	**3**	**i=3**	**3**	-35.4	0.007	0.007	0.001	0.007	0.1
	4	**i=2**	**2**	-41.1	0.009	0.009	0.001	0.009	1.5

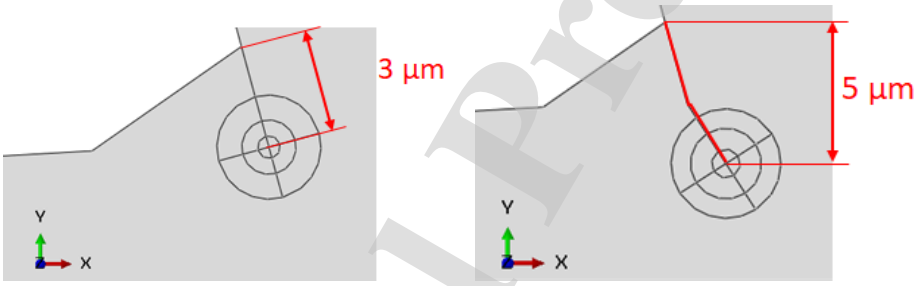

(a) (b)

Figure 7: FE analysis for Pook's approach verification [55]: a) 3 μm- long crack in multiaxial condition starting from a critical valley ; b) crack branching: a branch crack (in mode I) starts from the main crack (total crack depth of 5 μm)

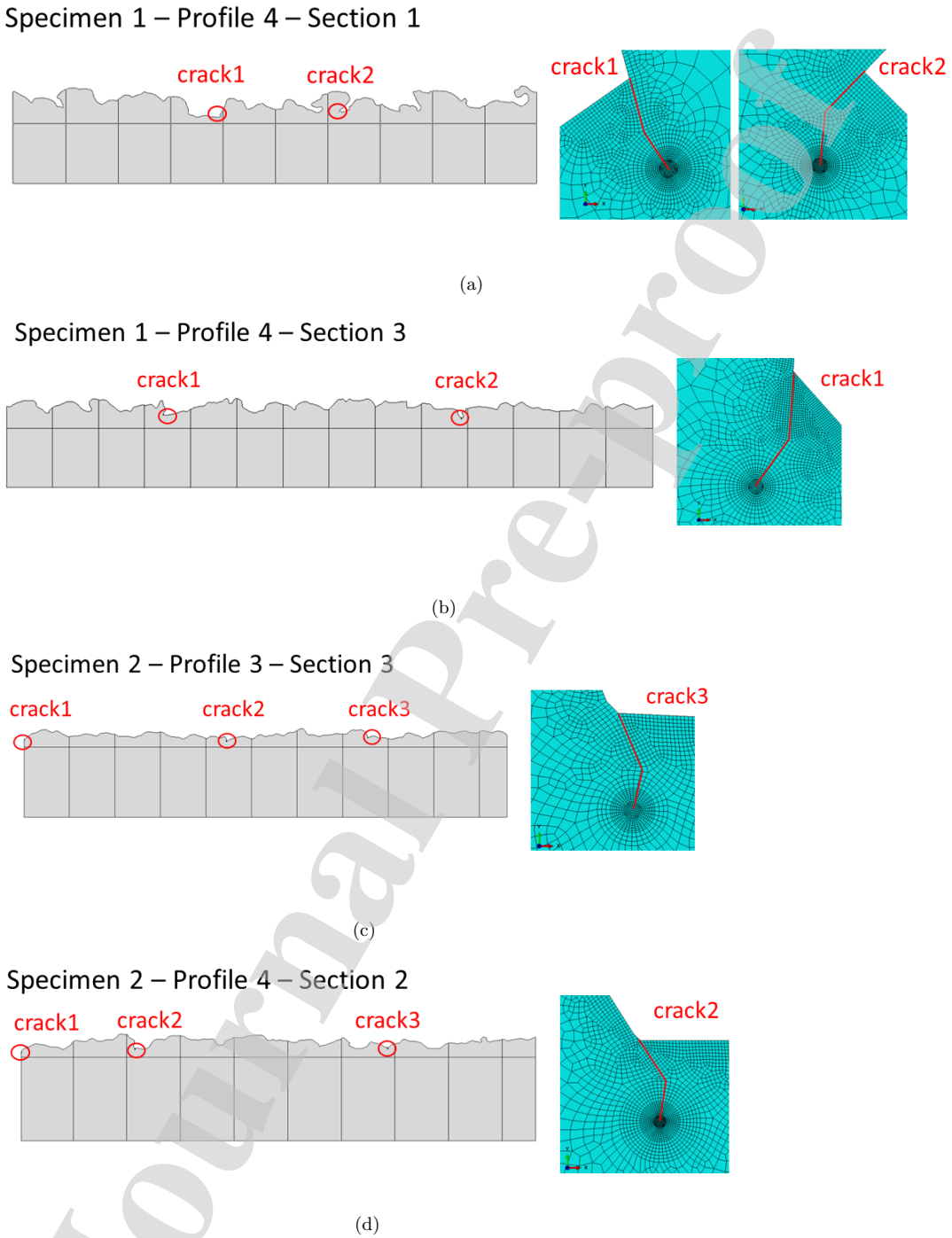

Figure 8: Cases (a, b, c, d) of cracks selected with significant effect of multiaxiality with $\frac{K_{II,FEA}}{K_{I,FEA}} \geq 10\%$. Left: sections of real surface profile (2.5 mm sample). Right: details of accurate FE model for crack branching .

5. Results of SIF for 2D cracks

5.1. Geometric factor extraction from FE analysis results

As described in Sect. 4.2, each "critical" valley of the different sections (an average of 3 locations per section, for a total of 102 locations) was modelled as an equivalent crack with total depth $a = 5\,\mu\text{m} + d_v$, where d_v is the valley depth calculated as the difference between the primary and the waviness profile.

The geometric factor $F_{\theta,FEA}$ was then obtained from FE SIF results $K_{\theta,FEA}$ (see Sect. 4.3) as:

$$F_{\theta,FEA} = \frac{K_{\theta,FEA}}{\sigma\sqrt{\pi a}} \tag{3}$$

where σ=1 MPa is the stress range applied in the FE analysis.

5.2. Distribution of the geometric factor

A histogram of frequency of $F_{\theta,FEA}$ results for the profiles filtered with the two cut-off wavelengths $\lambda_c = 0.8mm$ and $\lambda_c = 2.5mm$ is displayed in Fig. 9.a. The histograms show two very dispersed distributions.

The same results are also plotted in terms of a multiaxiality factor ($K_{II,FEA}/K_{I,FEA}$) in Fig. 9.b. As can be seen, $F_{\theta,FEA}$ does not depend on the multiaxiality factor ($K_{II,FEA}/K_{I,FEA}$), which (on the other hand) rarely exceeds the 10 %. Therefore multiaxiality is not the parameter that controls the scatter of the geometric factor $F_{\theta,FEA}$.

There are two potential sources of variability of the $F_{\theta,FEA}$:

- The valley depth d_v depends on the reference line chosen for the measurement. In some cases, d_v may be underestimated or overestimated, as a consequence of how the load lines are distributed in the rough surface (in relation to to the reference waviness profile).
- The effect of shielding due to the sequence of depressions and protrusions of the rough surface.

These effects are going to be discussed in Sect. 6.

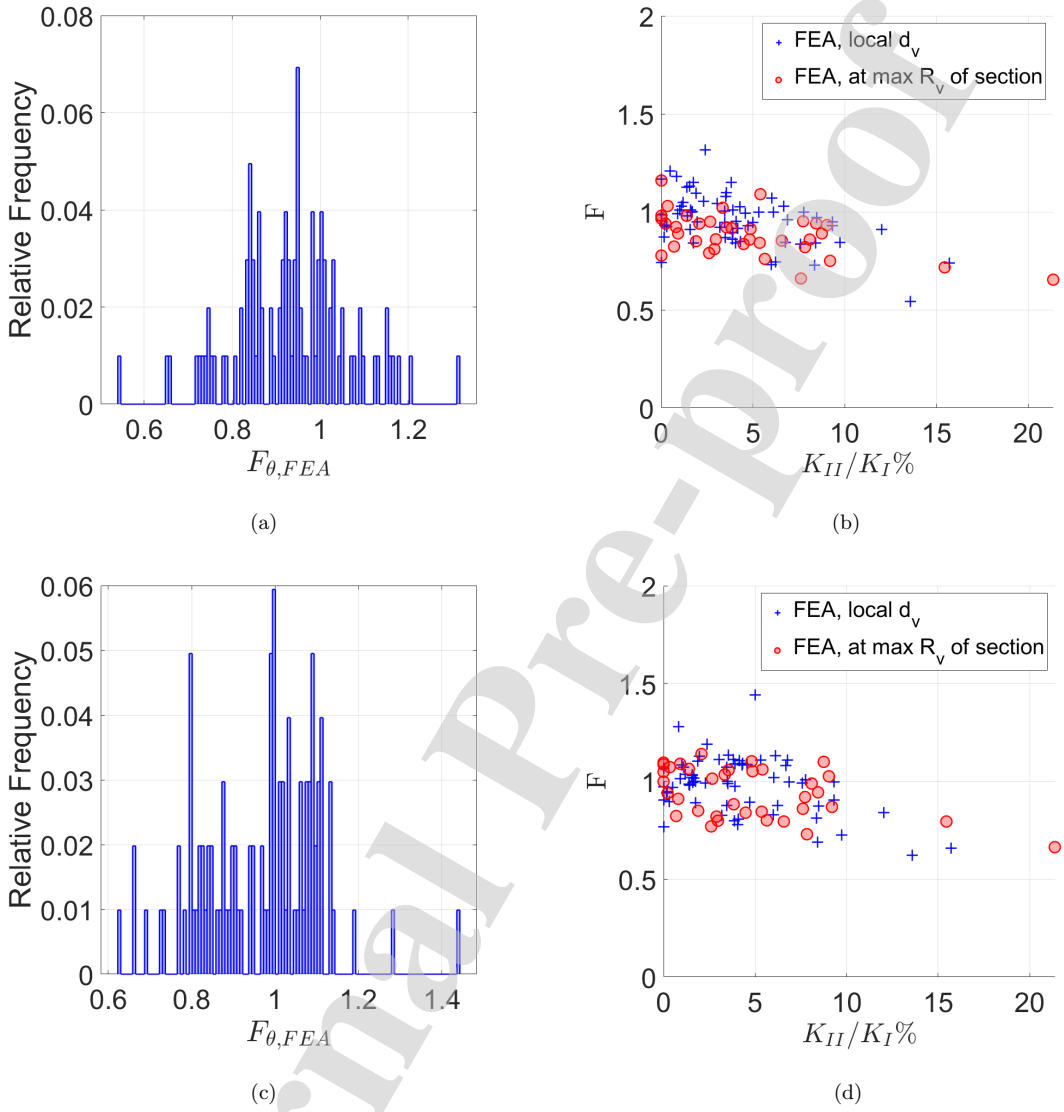

Figure 9: Results of FE analyses: a) histogram geometric factor data $F_{\theta,FEA}$ for profiles filtered with $\lambda_c = 2.5mm$; b) $F_{\theta,FEA}$ data plotted in terms of a multiaxiality factor $(K_{II,FEA}/K_{I,FEA})\,\%$ with $\lambda_c = 2.5mm$; c) histogram geometric factor data $F_{\theta,FEA}$ for profiles filtered with $\lambda_c = 0.8mm$; d) $F_{\theta,FEA}$ data plotted in terms of a multiaxiality factor $(K_{II,FEA}/K_{I,FEA})\,\%$ with $\lambda_c = 0.8mm$

6. Discussion

6.1. Evaluation of the theoretical geometric factor

Murakami's relationships Eqs.4, 5, modelling the effect of surface roughness on fatigue properties, were adopted in this study in order to investigate the shielding effect on the cracks' SIF extracted from FE analysis results.

$$\frac{\sqrt{area_R}}{b} \cong 0.97\left(\frac{a}{b}\right) - 3.51\left(\frac{a}{b}\right)^2 - 9.74\left(\frac{a}{b}\right)^3 \qquad \text{for } 0 < \frac{a}{b} < 0.195 \qquad (4)$$

$$\frac{\sqrt{area_R}}{b} \cong 0.38 \qquad \text{for } 0.195 < \frac{a}{b} < 3 \qquad (5)$$

It is important to underline that Murakami introduced these relationships to model a periodic surface (a turned surface of rolled steel bars) as a periodic series of 2D cracks, while AM as-built surfaces are complex and irregular.
The following choices were made for our particular application of this model:

- An equivalent crack with total depth $a = 5\,\mu\text{m} + d_v$ was considered. The valley depth at the location of the crack, d_v, is measured as the difference between the primary profile and the reference line (that are the waviness profile for the filtered cases and the section's mean line for the unfiltered one).

- The pitch b of the equivalent artificial roughness is the R_{Sm} average spacing parameter of the section, as already stated in Sect. 4.1.

  The spacing average is made on the spacing between all valley-valley sequences present in the section, where valleys are taken into account if they within certain bounds delimited by user-defined vertical thresholds (See Appendix). For instance, we adopted the suggested thresholds: $H_l = 10\%R_v$ (lowerbound), $H_u = 10\%R_p$ (upperbound).

The theoretical geometric factor $F_{t????heor}$ was calculated as (Eq. 6):

$$F_{theor} = 0.65\sqrt{\frac{\sqrt{area_R}}{a}} \qquad (6)$$

6.2. Significant cases for the profile filtering effect

Some significant crack locations have been chosen results for showing how profile filtering affects the valley depth measurements, and consequently the calculated geometric factor $F_{\theta,FEA}$. The crack locations are shown in Fig. 10 and the corresponding data for the geometric factor (expressed by $F_{\theta,FEA}$ and F_{theor}) is listed in Table 3.

The black solid line in Fig. 10 is the primary profile of a section with a length of 2.5 mm ("section 3" of "profile 1" extracted from specimen 2). The zero line (dashed black line) is the mean line of the whole primary profile. The blue solid line is the waviness profile of the section, obtained after application of the Robust Gauss filter on the whole primary profile with cut-off wavelength $\lambda_c = 2.5mm$. The magenta solid line is the waviness profile obtained after filtering with cut-off wavelength $\lambda_c = 0.8mm$.

For the sake of completeness, also the mean line of the primary section's profile is displayed as a dashed blue line , which is the reference line for the unfiltered profile.

Isolated cracks

Fig. 10.a shows a profile with all cracks that are almost isolated (distance in relation to other cracks $> 5a$).

For instance, we would expect that *crack1*, that is an isolated crack, should have a geometric factor close to 1.12 (like an edge crack in a semi-infinite plate). Instead, the corresponding results in Table 3 show a low F, close to 0.9, for the filtering with $\lambda_c = 2.5mm$ or the unfiltered profile. However, in this case F reduction is not due to the shielding but to the fact that the reference line (i.e. the blue waviness line for the filtered profile with $\lambda_c = 2.5mm$, or the blue dashed mean line for the unfiltered profile) is too high compared to the real surface profile. The situation changes considerably if we look at $F_{\theta,FEA}$ values for filtering with $\lambda_c = 0.8mm$. Taking the magenta waviness line as a reference, the valley depth where *crack1* is located decreases and $F_{\theta,FEA}$ increases up to 1.1.

If we observe *crack2*, another isolated crack, we can see that $F_{\theta,FEA} = 1.3$ for both

the unfiltered profile and the one filtered with $\lambda_c = 2.5mm$. In this case too this is due to the fact that the reference line is misplaced. The reference line should stand much higher than the mean line because there is a protrusion, so the measured valley depth is shorter than the depth of the actual notch that leads to stress concentration. For filtering with $\lambda_c = 0.8mm$, $F_{\theta,FEA}$ is reduced to 1.2, because the magenta waviness follows the macroscopic deviations more closely.

Also *crack3* is an isolated crack with $F_{\theta,FEA} \approx 1$ for the filtered profiles, while $F_{\theta,FEA}$=0.9 for the unfiltered profile. The only crack that is described well for all the filtering cases is *crack4*, with $F_{\theta,FEA}$=1 close to 1.12.

Considering the theoretical geometrical factor, F_{theor} calculated for the profile filtered with $\lambda_c = 2.5mm$, show that all the cracks are unshielded, as values are close to 1. Instead, the theoretical value for *crack2* is F_{theor}=0.61 due to the incorrect calculation of the average spacing b with $\lambda_c = l_s = 0.8mm$. The wrong a/b ratio of nearly 0.5 (much higher than the a/b ratio calculated with $\lambda_c = 2.5mm$) leads to a wrong theoretical description of *crack2* that would be taken as being shielded.

Shielded cracks

Fig. 10.b shows a profile that was chosen because there is one isolated crack (*crack1* that is at the root of deepest valley of the section, with $F_{\theta,FEA}$ close to 1), while other cracks are surrounded by valleys with similar depths and therefore affected by shielding ($F_{\theta,FEA}$ close to 0.7-0.8). Once again, for all three cracks, there is a small effect on $F_{\theta,FEA}$ due to the different values of d_v for the two filters.

The description of the shielding effect by the theoretical Murakami's equation is not so good, because F_{theor} values are too high with $\lambda_c = 2.5mm$ (every crack is almost unshielded) or too low with $\lambda_c = 0.8mm$ (every crack is severely shielded). Again, this is due to a significant effect of the filtering on R_{Sm} that leads to erratic values of a/b.

Summary of observations

The analysis of single cracks allowed us to understand different effects:

- The evaluation of F (from both FE analysis and the theoretical one) is influenced by the reference profile, as a consequence of the profile filter adopted, because it affects the cracks depth (or profile depth);
- The theoretical geometrical factor F_{theor} is strongly influenced by the definition of the *spacing* which, once again, depends on the profile filtering and the method for its calculation. This is a key factor and usually it is not considered by analyses based on stress concentration [23, 24, 56].

These effects, combined with the random nature of the as-built surface features, suggest that any evaluation of the shielding effects by $F_{\theta,FEA}$ cannot be made without a statistical analysis.

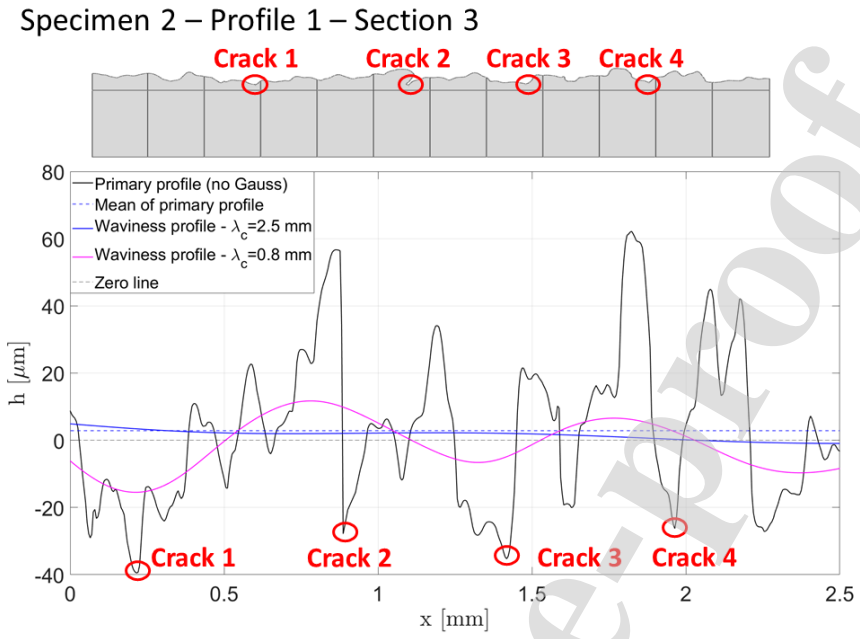

(a)

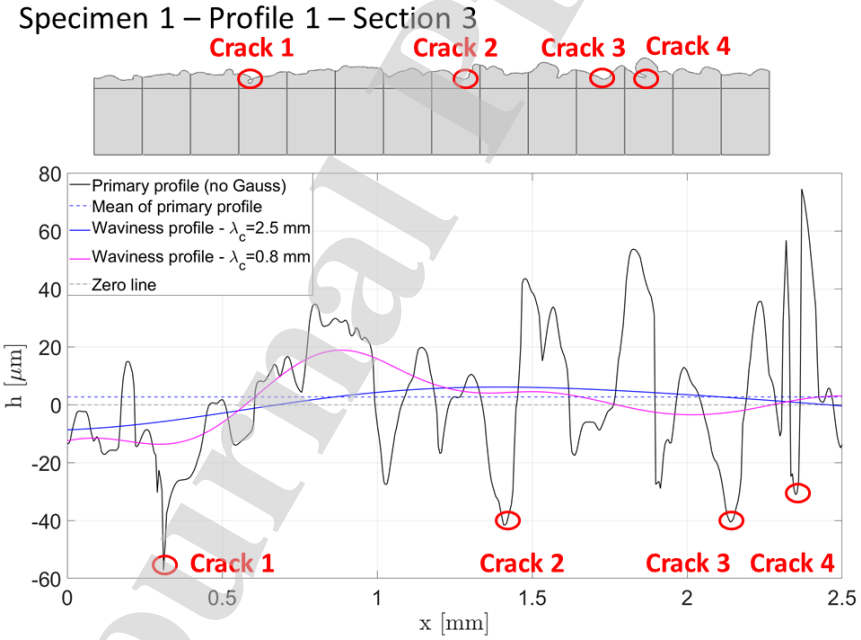

(b)

Figure 10: Significant cases for the analysis of SIF (data in Table 3): a) isolated cracks; b) cracks affected by shielding effect (cracks 2-3-4 are close to other valleys with similar depth).

Table 3: Profile filtering effect: a) case with $F > 1.12$ (Fig. 10.a), b) case with evident shielding effect (Fig. 10.b)

Case	**Specimen**	**Profile**	**Section**	**Crack**	$\frac{K_{II}}{K_I}\%$		$F_{\theta,FEA}$	F_{theor}	$\frac{a}{b}$
a)	**2**	**1**	**i=3**	**1**	4.81	$\lambda_c = 0.8$ **mm**	1.1	1.05	0.08
						$\lambda_c = 2.5$ **mm**	0.86	0.94	0.17
						Unfiltered	0.86	0.86	0.22
				2	2.39	$\lambda_c = 0.8$ **mm**	1.19	0.61	0.43
						$\lambda_c = 2.5$ **mm**	1.32	1	0.12
						Unfiltered	1.3	0.95	0.16
				3	3.9	$\lambda_c = 0.8$ **mm**	0.98	1	0.13
						$\lambda_c = 2.5$ **mm**	0.89	0.97	0.15
						Unfiltered	0.89	0.9	0.2
				4	3.8	$\lambda_c = 0.8$ **mm**	1.11	1	0.125
						$\lambda_c = 2.5$ **mm**	1.15	1.02	0.11
						Unfiltered	1.11	0.96	0.16
b)	**1**	**1**	**i=3**	**1**	3.9	$\lambda_c = 0.8$ **mm**	1.09	0.58	0.48
						$\lambda_c = 2.5$ **mm**	1.01	0.93	0.18
						Unfiltered	0.94	0.74	0.29
				2	2.89	$\lambda_c = 0.8$ **mm**	0.82	0.74	0.3
						$\lambda_c = 2.5$ **mm**	0.81	0.95	0.17
						Unfiltered	0.84	0.85	0.22
				3	0.85	$\lambda_c = 0.8$ **mm**	0.82	0.59	0.47
						$\lambda_c = 2.5$ **mm**	0.77	0.97	0.15
						Unfiltered	0.82	0.94	0.17
				4	5.98	$\lambda_c = 0.8$ **mm**	0.83	0.63	0.4
						$\lambda_c = 2.5$ **mm**	0.73	0.97	0.15
						Unfiltered	0.68	0.76	0.28

6.3. Comparison between theoretical and FEA results

The dispersed $F_{\theta,FEA}$ data extracted from the FEA analyses is reported in Fig. 11 on Murakami's plot (Fig. 1, Sect. 1) of the geometric factor as a function of the ratio a/b [36]. The theoretical curve is displayed in Fig. 11.a and Fig. 11.c as a black solid line. FE analysis (F_{θ,FEA_j}, $(a/b)_j$) data points are represented by blue markers if the crack is positioned at a generic valley or by red markers at the deepest valley in a 2.5 mm section (note that here the deepest valleys are also counted as "generic valleys" whenever the cracks are all analysed together).

The first observation is that the most erratic $F_{\theta,FEA}$ values belong to generic valleys and not to the largest values. Then, it is evident that data points (for both filtering cut-off wavelengths) somehow follow the trend of the theoretical curve: the geometric factor $F_{\theta,FEA}$ decreases with a/b, but the scatter of FE data is as important as the dependence of the geometric factor on a/b.

It is thus important to understand how FE analysis data deviate from the theoretical curve. This was done by calculating mean and standard deviation of the error ϵ, defined for a single crack j as:

$$\epsilon_j = (F_{\theta,FEA_j} - F_{theor_j}) \tag{7}$$

where F_{θ,FEA_j} and F_{theor_j} are the values for the $j-th$ crack considered. The mean and scatter of the error ϵ, together with mean values of the two distributions of the geometric factor ($\overline{F}_{\theta,FEA}$= mean of the distribution of F_{θ,FEA_j} and $\overline{F}_{theor}$ mean of the distribution of F_{theor_j}) related to the maximum valley depths within 2.5 mm-sections are reported in Table 4.

We also analysed the correlation between the $F_{\theta,FEA}$, F_{theor} variables by fitting the data with a bivariate Gaussian distribution: again, this is done by considering solely the cracks placed at the deepest valley in a 2.5 mm-sections. The bivariate distributions for λ_c=2.5 mm and λ_c=0.8 mm are shown in Fig. 11.b and 11.d respectively and the correlation coefficient ρ is also reported in Tab. 4.

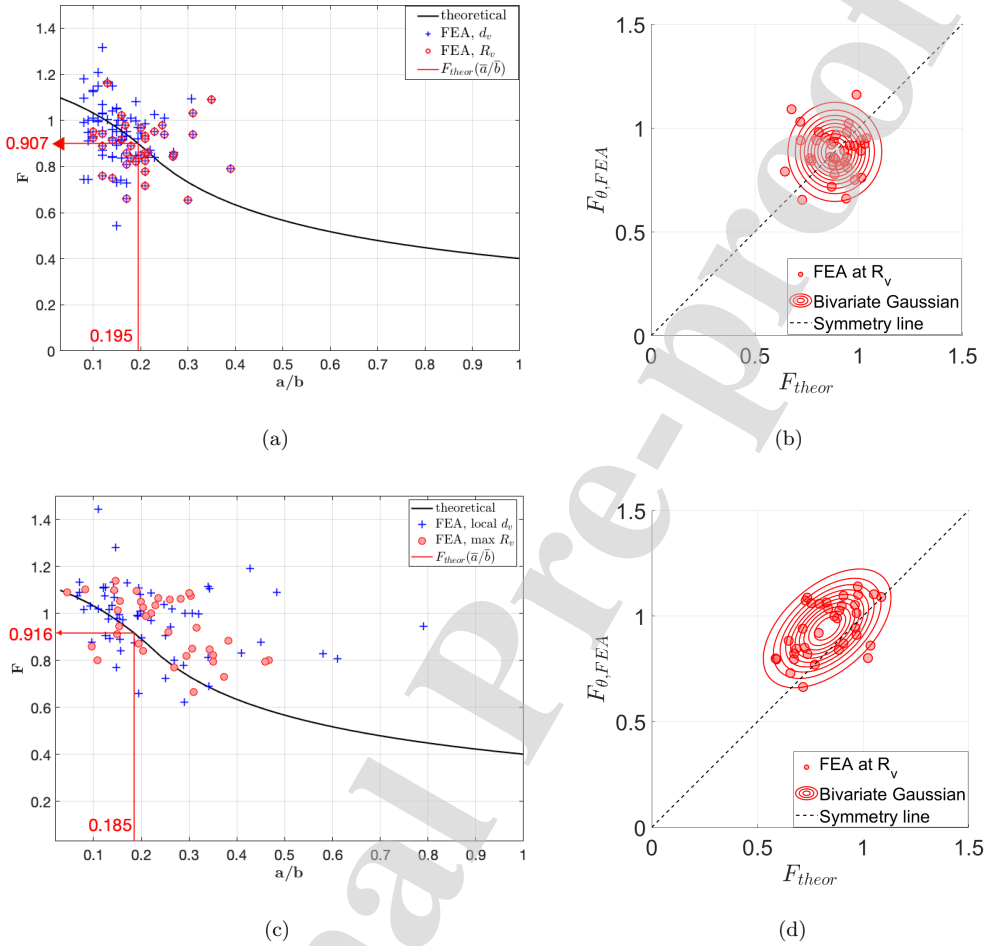

Figure 11: Comparison of estimated SIFs with theoretical curve: a) trend of the geometric factor $F_{\theta,FEA}$ vs ratio "a/b" for the filtered profile with $\lambda_c = 2.5mm$; b) correlation between $F_{\theta,FEA}$ and F_{theor} $\lambda_c = 2.5mm$; c) trend of the geometric factor $F_{\theta,FEA}$ vs ratio "a/b" for the filtered profile with $\lambda_c = 0.8mm$; correlation between $F_{\theta,FEA}$ and F_{theor} $\lambda_c = 0.8mm$ (blue=data for generic valley depths d_v, red= data for valleys with depth R_v).

Table 4: Scatter and mean value of the distribution of the geometric factor evaluated at the valleys with max depth R_v

	$\lambda_c = 2.5$ mm	$\lambda_c = 0.8$ mm
μ_ϵ	0.036	0.13
σ_ϵ	0.153	0.200
$\overline{F}_{\theta,FEA}$	0.885	0.942
$\overline{F}_{theor}$	0.886	0.83
ρ	0.002	0.51
$\overline{a}/\overline{b}$	0.195	0.185
$F_{theor}(\overline{a}/\overline{b})$	0.907	0.916

By looking at Tab. 4, we can see that μ_ϵ and σ_ϵ are lower for λ_c=2.5 mm: this fact, together with the erratic values of blue data points in Fig. 11.c, would lead to the wrong conclusion that this is the best filter.

Actually, the correlation figures show a very different situation: the perfectly circular shape of the contours for the case with λ_c=2.5 mm indicates no correlation at all (as confirmed a correlation coefficient $\rho \approx 0$). This means that there is no possibility to correctly predict F for any single deep profile valley (the R_v values).

On the contrary, the filtered case with λ_c=0.8 mm shows a significant correlation between numerical and theoretical results: the correlation coefficient is ρ=0.51 and the shape of the multivariate contours are elongated along the direction of the symmetry line. This positive effect is due to the fact that the error on d_v is reduced, with a waviness line that better follows the profile fluctuations as reference line for the profile depth measurements (as shown in Sect. 6.2).

6.4. Predictability of the the F factor

Eventually from the plots in Fig. 11, the conclusion that can be drawn is that the local shielding effect is not precisely estimated by the theoretical shielding model model for single cracks. The lack of precision is due to the complex and irregular random surface, which on one hand is far from the assumptions of *regularly spaced* micro-notches used for the model, and, on the other hand, is subjected to the filtering effects already discussed in Sect. 6.2 .

However, it is interesting to estimate the geometric factor F through the ratio $\overline{a}/\overline{b}$, where $\overline{a} = mean(R_v)$ (average R_v for the red data points) and $\overline{b} = mean(R_{sm})$ (average of the mean width of the elements in each section). In detail (results are reported again in Tab. 4), it can be observed that, even in presence of a significant scatter, the estimated value of the geometric factor (for both filters) is close to $\overline{F}_{\theta,FEA}$. Moreover, both the estimates are close to $\overline{F}$=0.9, which is an average geometric factor often adopted in literature (see for example by [5], [26],[28]).

This is an interesting result, valid for our as-built surfaces where the profile waviness is only due to L-PBF random deposition, without significant *stair-case* or macrogeometrical effects.

7. Conclusions

In this work μCT scan data was used to analyse the shielding effect ahead of prospective cracks of L-PBF cylindrical surfaces. 2D FE models were extracted from 2D diametral sections of the 3D reconstruction by the μ-CT of two fatigue specimens. The recontructed profiles were analysed with the Robust Gauss filter with two different cut-off wavelengths ($\lambda_c = 0.8mm$ and $\lambda_c = 2.5mm$) to assess the impact of the filtering choice. The major depressions below the reference profiles were modelled by FE by adding a 5 micron crack to obtain the SIF in different significant crack locations along the profiles and compare it with theoretical formulation of shielding factor dependent on depth/pitch ratio.
The main conclusions that we can draw from the numerical-theoretical comparison and from some significant cases for the shielding (shown in Sect. 6.2) are:

1. The scatter of FE results around the theoretical shielding curve is very large. One reason for the poor local description is the choice of a reference profile for the valley depth measurements that does not accurately accommodate how the load lines are distributed in the material. Another reason is the complex choice of a spacing parameter to represent how close the valleys have to be in order to be shielded in terms of SIF.
2. The correlation between numerical and theoretical results increases with a proper choice of the reference profile for the valley depth measurements. In our case, a better correlation is found for the profile filtered with $\lambda_c = 0.8mm$ (which is the value suggested by standards for our R_{Sm}). This is due to the fact that the valley depths are measured more accurately within relation to the reference line.
3. Even if the scatter prevents precise description of the *local shielding* for any crack, Murakami's shielding model is still valid for an irregular complex surface as far as the average shielding effect is concerned (in terms of the average value of geometric factor).

Acknowledgements

Support by the Italian Ministry for Education, University and Research through the Department of Excellence project LIS4.0 (Lightweight and Smart Structures for Industry 4.0) is gratefully acknowledged.

The authors want to thank ESA, in the person of Dr. J. Gumpinger, for permission to use data and specimen supply, together with E. Beevers for careful CT scans.

Declaration of Competing Interest

The authors declare that they have no known competing financial interests or personal relationships that could have appeared to influence the work reported in this paper.

Appendix A: Spacing parameter R_{Sm}

Seewig et al. [52] stated that current standards for profile measurements of roughness parameters lack an unambiguous characterization of the spacing of the examined profile. The standard roughness parameter R_{Sm} (roughness spacing mean) is defined as the "mean value of the profile element widths, X_s, within a sampling length" [47]:

$$R_{Sm} = \frac{1}{m} \sum_{i=1}^{m} X_{S_i} \tag{8}$$

where a profile element is a peak-valley or valley-peak sequence. The issues with this definition are:

- "Zero elements" (neither peaks nor valleys, continuous profile portions on the reference line) of the profile are not considered.
- The implementation of this definition is ambiguous and results of different sets of measurements are not comparable.

To overcome these issues, Seewig et al. implemented an algorithm to distinguish the "profile features" unambiguously, so that a clear feature-based definition of the R_{Sm} parameter could be given. Once the reference line is defined (in this case the reference line is the zero line for the roughness profile), segmentation of the profile features is based on "zero-crossings".

A zero-crossing is detected whenever two adjacent profile points (within a bounded "region of doubt" $[-O_D, O_H]$ around the reference line) are connected by a segment (with a positive, negative or zero slope) that intersects the zero line. At this point, the profile feature can be classified as hill (i.e. peak), dale (i.e. valley), or zero element: we have a hill if at least one profile sample is equal or greater than O_H, a dale if at least one profile sample is equal or lower than O_D, otherwise we have a zero-element.

To remove non-relevant elements, two different vertical thresholds are used for dale (H_l) and hill (H_u). These thresholds are usually higher than the bounds O_D, O_H of the zero-crossing region of doubt. For computing R_{Sm} and R_c parameters, they suggest the following thresholds (that were used for calculating the parameters in Sect. 3):

- Vertical thresholds: $H_u = 10\%R_p$, $H_l = 10\%R_v$;
- Limits for the zero crossings: $O_H = 0.01\%R_p$, $O_D = 0.01\%R_v$.

The last step of the algorithm involves merging adjacent features of the same type with each other.

A profile element is thus defined as a portion between the zero-crossings of the profile and R_{Sm} is calculated using Eq. (8).

References

[1] M. Gorelik, Additive manufacturing in the context of structural integrity, International Journal of Fatigue 94 (2017) 168–177.

[2] J. Mochache, L. Weihmuller, D. Duprat, V. Chahal, R. M. Taylor, A review of fatigue and damage tolerance life prediction methodologies towards certification of additively manufactured metallic principal structural elements, AIAA Scitech 2021 Forum (2021) 1–23.

[3] A. Yadollahi, N. Shamsaei, Additive manufacturing of fatigue resistant materials: Challenges and opportunities, International Journal of Fatigue 98 (2017) 14–31.

[4] A. Fatemi, R. Molaei, J. Simsiriwong, N. Sanaei, J. Pegues, B. Torries, N. Phan, N. Shamsaei, Fatigue behaviour of additive manufactured materials: An overview of some recent experimental studies on Ti-6Al-4V considering various processing and loading direction effects, Fatigue and Fracture of Engineering Materials and Structures 42 (5) (2019) 991–1009.

[5] R. Molaei, A. Fatemi, N. Sanaei, J. Pegues, N. Shamsaei, S. Shao, P. Li, D. H. Warner, N. Phan, Fatigue of additive manufactured Ti-6Al-4V, Part II: The relationship between microstructure, material cyclic properties, and component performance, International Journal of Fatigue 132 (2020).

[6] I. Koutiri, E. Pessard, P. Peyre, O. Amlou, T. De Terris, Influence of SLM process parameters on the surface finish, porosity rate and fatigue behavior of as-built Inconel 625 parts, Journal of Materials Processing Technology 255 (2018) 536–546.

[7] M. Seifi, M. Gorelik, J. Waller, N. Hrabe, N. Shamsaei, S. Daniewicz, J. J. Lewandowski, Progress towards metal additive manufacturing standardization to support qualification and certification, Jom 69 (3) (2017) 439–455.

[8] E. Wycisk, A. Solbach, S. Siddique, D. Herzog, F. Walther, C. Emmelmann, Effects of defects in laser additive manufactured Ti-6Al-4V on fatigue properties, Physics Procedia 56 (C) (2014) 371–378. doi:10.1016/j.phpro.2014.08.120.

[9] S. Beretta, S. Romano, A comparison of fatigue strength sensitivity to defects for materials manufactured by AM or traditional processes, International Journal of Fatigue 94 (2017) 178–191. doi:10.1016/j.ijfatigue.2016.06.020.

[10] Y. Murakami, T. Takagi, K. Wada, H. Matsunaga, Essential structure of S-N curve: Prediction of fatigue life and fatigue limit of defective materials and nature of scatter, International Journal of Fatigue 146 (2021).

[11] Z. Wu, S. Wu, J. Bao, W. Qian, S. Karabal, W. Sun, P. J. Withers, The effect of defect population on the anisotropic fatigue resistance of AlSi10Mg alloy fabricated by laser powder bed fusion, International Journal of Fatigue 151 (2021).

[12] Y. Murakami, M. Endo, Effects of defects, inclusions and inhomogeneities on fatigue strength, International Journal of Fatigue 16 (3) (1994) 163–182. doi:10.1016/0142-1123(94)90001-9.

[13] S. Romano, A. Brückner-Foit, A. Brandão, J. Gumpinger, T. Ghidini, S. Beretta, Fatigue properties of AlSi10Mg obtained by additive manufacturing: Defect-based modelling and prediction of fatigue strength, Engineering Fracture Mechanics 187 (2018) 165–189. doi:10.1016/j.engfracmech.2017.11.002.

[14] P. D. Nezhadfar, R. Shrestha, N. Phan, N. Shamsaei, Fatigue behavior of additively manufactured 17-4 PH stainless steel: Synergistic effects of surface roughness and heat treatment, International Journal of Fatigue 124 (2019) 188–204.

[15] R. Molaei, A. Fatemi, N. Phan, Significance of hot isostatic pressing (HIP) on multiaxial deformation and fatigue behaviors of additive manufactured Ti-6Al-4V including build orientation and surface roughness effects, International Journal of Fatigue 117 (2018) 352–370.

[16] D. Greitemeier, C. Dalle Donne, F. Syassen, J. Eufinger, T. Melz, Effect of surface roughness on fatigue performance of additive manufactured Ti–6Al–4V, Materials Science and Technology (United Kingdom) 32 (7) (2016) 629–634. doi:10.1179/1743284715Y.0000000053.

[17] Z. Chen, S. Cao, X. Wu, C. H. Davies, Surface roughness and fatigue properties of selective laser melted Ti-6Al-4V alloy, Additive Manufacturing for the Aerospace Industry (2019) 283–299.

[18] G. Nicoletto, R. Konečná, Influence of surface orientation and segmentation on the notch fatigue behavior of as-built DMLS Ti6Al4V, Structural Integrity 7 (2019) 107–113.

[19] F. Cabanettes, A. Joubert, G. Chardon, V. Dumas, J. Rech, C. Grosjean, Z. Dimkovski, Topography of as built surfaces generated in metal additive manufacturing: A multi scale analysis from form to roughness, Precision Engineering 52 (2018) 249–265.

[20] S. Bagehorn, J. Wehr, H. J. Maier, Application of mechanical surface finishing processes for roughness reduction and fatigue improvement of additively manufactured Ti-6Al-4V parts, International Journal of Fatigue 102 (2017) 135–142.

[21] M. H. Nasab, D. Gastaldi, N. F. Lecis, M. Vedani, On morphological surface features of the parts printed by selective laser melting (SLM), Additive Manufacturing 24 (2018) 373–377.

[22] T. Persenot, A. Burr, G. Martin, J. Y. Buffiere, R. Dendievel, E. Maire, Effect of build orientation on the fatigue properties of as-built Electron Beam Melted Ti-6Al-4V alloy, International Journal of Fatigue 118 (2019) 65–76. doi:10.1016/j.ijfatigue.2018.08.006.

[23] J. W. Pegues, N. Shamsaei, M. D. Roach, R. S. Williamson, Fatigue life estimation of additive manufactured parts in the as built surface condition, Material Design and Processing Communications 1 (3) (2019) e36.

[24] W. Schneller, M. Leitner, S. Pomberger, S. Springer, F. Beter, F. Grün, Effect of post treatment on the microstructure, surface roughness and residual stress regarding the fatigue strength of selectively laser melted AlSi10Mg structures, Journal of Manufacturing and Materials Processing 3 (4) (2019). doi:10.3390/jmmp3040089.

[25] W. Schneller, M. Leitner, S. Pomberger, F. Grün, S. Leuders, T. Pfeifer, O. Jantschner, Fatigue strength assessment of additively manufactured metallic structures considering bulk and surface layer characteristics, Additive Manufacturing 40 (December 2020) (2021) 101930.

[26] M. Nakatani, H. Masuo, Y. Tanaka, Y. Murakami, Effect of Surface Roughness on Fatigue Strength of Ti-6Al-4V Alloy Manufactured by Additive Manufacturing, Procedia Structural Integrity 19 (2019) 294–301. doi:10.1016/j.prostr.2019.12.032.

[27] S. Beretta, M. Gargourimotlagh, S. Foletti, A. du Plessis, M. Riccio, Fatigue strength assessment of "as built" AlSi10Mg manufactured by SLM with different build orientations, International Journal of Fatigue 139 (2020).

[28] J. Zhang, A. Fatemi, Surface roughness effect on multiaxial fatigue behavior of additive manufactured metals and its modeling, Theoretical and Applied Fracture Mechanics 103 (2019).

[29] A. du Plessis, S. Beretta, Killer notches: The effect of as-built surface roughness on fatigue failure in AlSi10Mg produced by laser powder bed fusion, Additive Manufacturing 35 (2020).

[30] B. Vayssette, N. Saintier, C. Brugger, M. El May, E. Pessard, Numerical modelling of surface roughness effect on the fatigue behavior of Ti-6Al-4V obtained by additive manufacturing, International Journal of Fatigue 123 (2019) 180–195. doi:10.1016/j.ijfatigue.2019.02.014.

[31] B. Vayssette, N. Saintier, C. Brugger, M. El May, Surface roughness effect of SLM and EBM Ti-6Al-4V on multiaxial high cycle fatigue, Theoretical and Applied Fracture Mechanics 108 (2020) 102581.

[32] G.-W. Zeng, M. Monu, C. Lupton, B. Lin, J. Tong, Towards a fundamental understanding of the effects of surface conditions on fatigue resistance for safety-critical AM applications, Int. J. Fatigue 136 (2020) 105585.

[33] T. D. Dinh, J. Vanwalleghem, H. Xiang, H. Erdelyi, T. Craeghs, W. Van Paepegem, A unified approach to model the effect of porosity and high surface roughness on the fatigue properties of additively manufactured Ti6-Al4-V alloys, Additive Manufacturing 33 (2020) 101139.

[34] R. Peterson, R. E.; Plunkett, Stress Concentration Factors, Journal of Applied Mechanics 42 (1) (1975) 248.

[35] D. Arola, M. Ramulu, An Examination of the Effects from Surface Texture on the Strength of Fiber Reinforced Plastics, Journal of Composite Materials 33 (2) (1999) 102–123.

[36] Y. Murakami, K. Takahashi, T. Yamashita, Quantitative evaluation of the effect of surface roughness on fatigue strength (Effect of depth and pitch of roughness), Nippon Kikai Gakkai Ronbunshu, A Hen/Transactions of the Japan Society of Mechanical Engineers, Part A 63 (612) (1997) 1612–1619.

[37] J. Gockel, L. Sheridan, B. Koerper, B. Whip, The influence of additive manufacturing processing parameters on surface roughness and fatigue life, International Journal of Fatigue 124 (2019) 380–388. doi:10.1016/j.ijfatigue.2019.03.025.

[38] A. Du Plessis, I. Yadroitsev, I. Yadroitsava, S. G. Le Roux, X-Ray Microcomputed Tomography in Additive Manufacturing: A Review of the Current Technology and Applications, 3D Printing and Additive Manufacturing 5 (3) (2018) 227–247.

[39] J. Y. Buffiere, Fatigue Crack Initiation and Propagation from Defects in Metals: Is 3D Characterization Important?, Procedia Structural Integrity 7 (2017) 27–32. doi:10.1016/j.prostr.2017.11.056.

[40] T. Persenot, A. Burr, R. Dendievel, J. Y. Buffière, E. Maire, J. Lachambre, G. Martin, Fatigue performances of chemically etched thin struts built by selective electron beam melting: Experiments and predictions, Materialia 9 (2020). doi:10.1016/j.mtla.2020.100589.

[41] A. du Plessis, P. Sperling, A. Beerlink, O. Kruger, L. Tshabalala, S. Hoosain, S. G. le Roux, Standard method for microCT-based additive manufacturing quality control 3: Surface roughness, MethodsX 5 (2018) 1111–1116.

[42] M. Hamidi Nasab, S. Romano, D. Gastaldi, S. Beretta, M. Vedani, Combined effect of surface anomalies and volumetric defects on fatigue assessment of AlSi7Mg fabricated via laser powder bed fusion, Additive Manufacturing 34 (2020).

[43] E. Beevers, A. D. Brandão, J. Gumpinger, M. Gschweitl, C. Seyfert, P. Hofbauer, T. Rohr, T. Ghidini, Fatigue properties and material characteristics of additively manufactured AlSi10Mg - Effect of the contour parameter on the microstructure, density, residual stress, roughness and mechanical properties, International Journal of Fatigue 117 (2018) 148–162.

[44] J. Gumpinger, A. D. Brandão, E. Beevers, T. Rohr, T. Ghidini, S. Beretta, S. Romano, Expression of Additive Manufacturing Surface Irregularities through a Flaw-Based Assessment, Structural Integrity of Additive Manufactured Parts (2020) 234–249.

[45] A. E739, Standard Practice for Statistical Analysis of Linear or Linearized Stress-Life ((2009).

[46] ASTM, Standard Practice for Conducting Force Controlled Constant Amplitude Axial Fatigue Tests of Metallic Materials (2002).

[47] ISO 4287:1997, Geometrical Product Specifications (GPS) - Surface texture: Profile method - Terms, definitions and surface texture parameters, International Organization for Standardization 1998 (1997) 1997–1998.

[48] BSI, ISO 4288:1998. Geometrical Product Specifications (GPS)- Surface texture: Profile method- Rules and procedures for the assessment of surface texture (1998).

[49] R. K. Leach, Surface topography characterization, in: Fundamental Principles of Engineering Nanometrology, 2010, pp. 211–262. doi:10.1016/b978-0-08-096454-6.10008-9.

[50] A. Daldossi, Surface features rating of as-built 3D printed parts for fatigue assessment, Ph.D. thesis (2019).

[51] S. Brinkman, H. Bodschwinna, Advanced Gaussian Filters, in: Advanced Techniques for Assessment Surface Topography: Development of a Basis for 3D Surface Texture Standards "Surfstand", 2003, pp. 63–90.

[52] J. Seewig, P. J. Scott, M. Eifler, B. Barwick, D. Hüser, Crossing - The-line segmentation as a basis for Rsm and Rc evaluation, Surface Topography: Metrology and Properties 8 (2) (2020).

[53] S. Carmignato, Accuracy of industrial computed tomography measurements: Experimental results from an international comparison, CIRP Annals - Manufacturing Technology 61 (1) (2012) 491–494.

[54] S. Courtin, C. Gardin, G. Bezine, H. B. H. Hamouda, Advantages of the j-integral approach for calculating stress intensity factors when using the commercial finite element software abaqus, Engineering Fracture Mechanics 72 (14) (2005) 2174–2185.

[55] L. Pook, Crack Paths, WIT Press, Southampton, 2002.

[56] S. Lee, B. Rasoolian, D. F. Silva, J. W. Pegues, N. Shamsaei, Surface roughness parameter and modeling for fatigue behavior of additive manufactured parts: A non-destructive data-driven approach, Additive Manufacturing (2021) 102094.

- As-built surfaces cause a significant fatigue debit for AM materials;
- An innovative analysis for the SIF ahead of surface features was applied;
- Results show that shielding effect is not perfectly described by current formulations valid for regularly spaced cracks

POLITECNICO
MILANO 1863

Milano, 9th April 2021

DIPARTIMENTO DI
MECCANICA

prof. Stefano Beretta

Author statement for manuscript:

" Analysis of the prospective SIF of cylindrical rough surfaces obtained by L-PBF "

by L. Barricelli and S. Beretta

The authors state that this work is not under consideration elsewhere and has not been published in any form before.

We approve the submission and declare no conflict of interests in this work.

The contributions to the paper:

1) L. Barricelli: FE analyses, manuscript preparation;

2) S. Beretta: project direction, manuscript preparation, manuscript revision.

On the behalf of the coauthors

Prof. Stefano Beretta

Dipartimento di Meccanica
Via La Masa, 1
20156 Milano

T +39 02 2399 8246
F +39 02 2399 8202
stefano.beretta@polimi.it
www.polimi.it

Partita Iva 04376620151
Codice Fiscale 80057930150

POLITECNICO
MILANO 1863

Milano, 9th April 2021

DIPARTIMENTO DI
MECCANICA

prof. Stefano Beretta

Author statement for manuscript:

" Analysis of the prospective SIF of cylindrical rough surfaces obtained by L-PBF "

by L. Barricelli and S. Beretta

The authors state that this work is not under consideration elsewhere and has not been published in any form before.

We approve the submission and declare no conflict of interests in this work.

The contributions to the paper:

1) L. Barricelli: FE analyses, manuscript preparation;

2) S. Beretta: project direction, manuscript preparation, manuscript revision.

On the behalf of the coauthors

Prof. Stefano Beretta

Dipartimento di Meccanica
Via La Masa, 1
20156 Milano

T +39 02 2399 8246
F +39 02 2399 8202
stefano.beretta@polimi.it
www.polimi.it

Partita Iva 04376620151
Codice Fiscale 80057930150